

pubs.acs.org/cm Article

# Structure and Magnetic Properties of Ni<sub>4</sub>V<sub>3</sub>O<sub>10</sub>, an Antiferromagnet with Three Types of Vanadium—Oxygen Polyhedra

Zachary W. Riedel, Fatemeh Amerikheirabadi, Kejian Qu, Jeffrey Huang, Mebatsion S. Gebre, Ankita Bhutani, Richard T. Haasch, Pinshane Y. Huang, André Schleife, and Daniel P. Shoemaker\*



Cite This: Chem. Mater. 2022, 34, 4721-4731



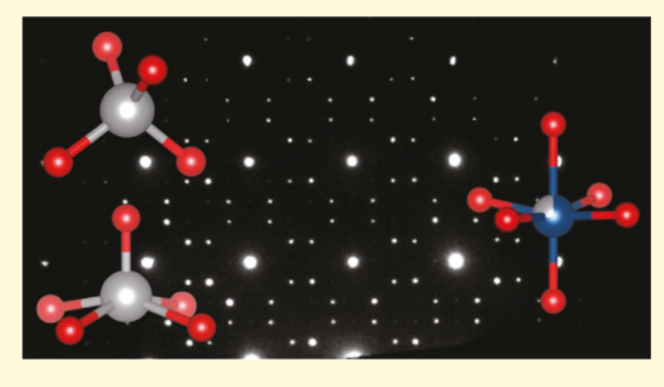
ACCESS

III Metrics & More



Supporting Information

ABSTRACT: The compound  $Ni_4V_3O_{10}$  forms a new structure type in the tetragonal space group P4/n. The material can be produced using solid-state synthesis in a narrow temperature range, and the structure was confirmed using X-ray and neutron powder diffraction data. The phase contains occupationally disordered Ni/V in regular-octahedral sites and V in tetrahedral and vanadyloctahedral sites. Bond valence and neutron/X-ray co-refinement data are compatible with three vanadium oxidation states  $(V^{3+}, V^{4+}, V^{5+})$  existing in the material, which would make it distinct in the Ni-V-O system and would place it in a small class of oxides with transition metals exhibiting three oxidation states. With a Néel temperature of 38 K and a Curie—Weiss parameter  $\theta = -234$  K, it displays frustrated antiferromagnetism evidenced by a broad hump



in the heat capacity below  $T_{\rm N}$ . The structure has a percolating distorted rock-salt-like network, leading to strong superexchange, but vanadyl-octahedral linkages frustrate magnetic ordering. The magnetic structure is assumed to be incommensurate, as simple propagation vectors can be ruled out by powder neutron diffraction.

# **■** INTRODUCTION

The Ni-V-O chemical system contains multiple ternary compounds with intriguing magnetic and electronic properties. Ni<sub>3</sub>V<sub>2</sub>O<sub>8</sub> forms a Kagomé staircase structure with four lowtemperature magnetic transitions<sup>1,2</sup> and has emerged as a component in new supercapacitors.<sup>3-6</sup> Both NiV<sub>3</sub>O<sub>8</sub>, a ferromagnet with transitions at 2 and 27 K,7 and Ni<sub>2</sub>V<sub>2</sub>O<sub>7</sub>, a 3D spin-1 antiferromagnet, have shown promising electrochemical properties for Li-ion battery applications. 9-12 Likewise, NiVO<sub>3</sub> and NiV<sub>2</sub>O<sub>6</sub> have demonstrated high, stable discharge capacities as anode materials in Li-ion batteries. 13,14 As a result, Li et al. have proposed using NiV2O6 as an electrode for flexible energy storage devices in wearable technology. 15 Another compound in the system, hematite-type  $V_{2-x}Ni_xO_3$  (0 < x < 0.75), is a wide solubility limit magnetic material with a tunable Mott transition temperature. 16,17 These phases are plotted in Figure 1.

Gianoglio and Ramonda reported an additional ternary phase close to these others in composition and designated it as Ni<sub>7</sub>V<sub>5</sub>O<sub>17</sub> based on their reactant powders' nominal Ni/V ratio and vanadium oxidation state. While *d*-spacings and relative intensities from X-ray diffraction data were reported for the new phase, its composition was not confirmed, the crystal structure was not determined, and the magnetic properties were not explored. Here, we show this phase to have an

approximate composition of Ni<sub>4</sub>V<sub>3</sub>O<sub>10</sub>, a unique structure type, and frustrated antiferromagnetic ordering.

# ■ EXPERIMENTAL PROCEDURE

**Synthesis.** The precursor powder mixture for  $Ni_4V_3O_{10}$  was prepared using two methods: high-impact mechanical ball milling or hand grinding with an agate mortar and pestle. For samples prepared using ball milling, a total of 2 g of powder of NiO (Alfa Aesar, 99%), V (Strem, 99.5%), and  $V_2O_5$  (Acros, 99.6%) were mixed under Ar in a stoichiometric ratio based on the chemical equation

20 NiO + 3 V + 6 
$$V_2O_5 \rightarrow 5Ni_4V_3O_{10}$$

Three stainless steel milling balls were used, with diameters of 0.5, 0.25, and 0.25 inches and with a combined mass of 10 g. The powders were sealed under Ar in a stainless steel jar and were milled for 1 h in a SPEX 8000D mixer mill under Ar. Next, the powders were drypressed at 465 MPa into pellets and loaded into a short quartz tube that was placed into a larger tube. During the subsequent vacuum sealing, this tube-in-tube design prevented contact between the heated quartz and V powder, which hardened the tube. Samples were then

Received: March 7, 2022 Revised: April 19, 2022 Published: May 9, 2022





Chemistry of Materials pubs.acs.org/cm Article

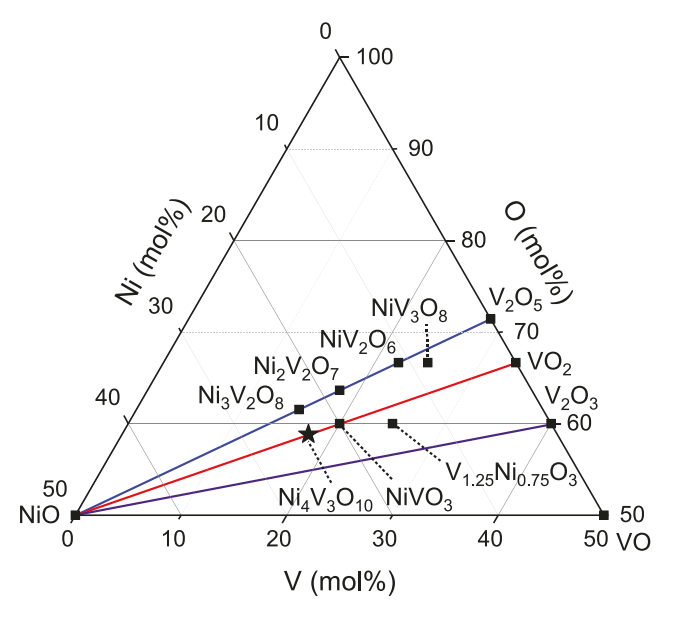


**Figure 1.** Truncated Ni–V–O phase diagram containing experimental phases near the composition of  $Ni_4V_3O_{10}$ . Lines indicate constant vanadium oxidation states (purple:  $V^{3+}$ , red:  $V^{4+}$ , blue:  $V^{5+}$ ).

heated at 10  $^{\circ}\text{C/min}$  to 800  $^{\circ}\text{C},$  where they were held for 72 h before quenching in an ice bath.

Samples were also prepared without ball milling. Using a mortar and pestle, a total of 2 g of the same precursor powders in the same proportions were ground together for 45 min under Ar. They were then pressed and sealed as before. After ramping to 800 °C at 10 °C/min, they were held for 144 h before being quenched in an ice bath. Pellets were then ground before repeating the pressing and sealing process. The new tube was then placed in a preheated, 800 °C oven. Three 144-h cycles were completed.

Additionally, to disentangle the effects of any hematite-type  $(V_{\nu}Ni)_2O_3$  impurities in the title compound, the impurity phase was synthesized using the same precursor powders in an approximate  $NiO/V/V_2O_5$  molar ratio of 335:199:233  $(V_{1.33}Ni_{0.67}O_3).$  The powders, totaling 0.5 g, were hand-ground with a mortar and pestle under Ar before dry-pressing and sealing in a quartz tube under vacuum. The sample was heated at 10 °C/min to 950 °C, the same temperature used by Rozier et al.,  $^{17}$  for 48 h before cooling naturally with the furnace over roughly 3 h.

**Characterization.** Room temperature X-ray powder diffraction data were collected at the Advanced Photon Source beamline 11-BM at Argonne National Laboratory ( $\lambda = 0.457913$  Å). Time-of-flight neutron powder diffraction data were collected at the POWGEN instrument at Oak Ridge National Laboratory's Spallation Neutron Source. Data collection occurred at 300 and 6.4 K, with additional data collected during cooling from 80 to 9 K at 0.8 K/min.

The crystal structure of  $Ni_4V_3O_{10}$  was initially solved using the parallel tempering global optimization algorithm in FOX<sup>19</sup> with the 11-BM X-ray powder diffraction data. Rietveld refinements to X-ray and neutron powder diffraction data were performed with GSAS-II. The Bilbao Crystallographic Server's PSEUDO<sup>21</sup> program guided crystallographic space group determination, and the server's MAXMAGN<sup>22</sup> program provided the maximal magnetic space groups for  $Ni_4V_3O_{10}$ . VESTA<sup>23</sup> was used for bond valence sum analysis of vanadium oxidation states, for crystal structure images, and for magnetic space group images. Bond valence sum parameters came from an analysis by Brown and Altermatt, <sup>24</sup> and the *B* parameter was set at 0.37 Å based on their analysis. For all BVS calculations, nickel and oxygen had fixed oxidation states of +2 and -2, respectively.

Magnetic property measurements were performed with powder mounted in a brass sample holder in a Quantum Design Magnetic Property Measurement System (MPMS3) vibrating sample magnetometer. For heat capacity measurements collected using a Quantum Design Physical Property Measurement System (PPMS), the powder was dry-pressed and mounted with Apiezon N-grease. Energy-dispersive X-ray fluorescence spectrometry (XRF) was performed on sample powders with a Shimadzu EDX-7000 spectrometer. A Kratos Axis Ultra, calibrated with Cu 2p<sub>3/2</sub> and Au 4f<sub>7/2</sub> standards, was used for X-ray photoelectron spectroscopy (XPS). Binding energy referencing was made to the C 1s peak (285.0 eV). A Cary 5000 spectrophotometer was used for UV—vis diffuse reflectance data.

A JEOL 6060LV scanning electron microscope equipped with an IXRF EDS elemental analysis system was used for micrographs and energy dispersive spectroscopy (EDS). A grain of  $\rm Ni_4V_3O_{10}$  was isolated within a sintered pellet using electron backscatter diffraction (EBSD) with a Thermo Scientific Scios2 DualBeam SEM/FIB and was cut from the bulk sample in an FEI Helios 600i DualBeam SEM/FIB. Electron energy loss spectroscopy (STEM-EELS) was performed on the grain with an FEI Themis Z Advanced Probe Aberration Corrected Analytical TEM/STEM.

## **■** COMPUTATIONAL PROCEDURE

First-principles simulations were performed using spin-polarized density functional theory  $(\mathrm{DFT})^{25}$  as implemented

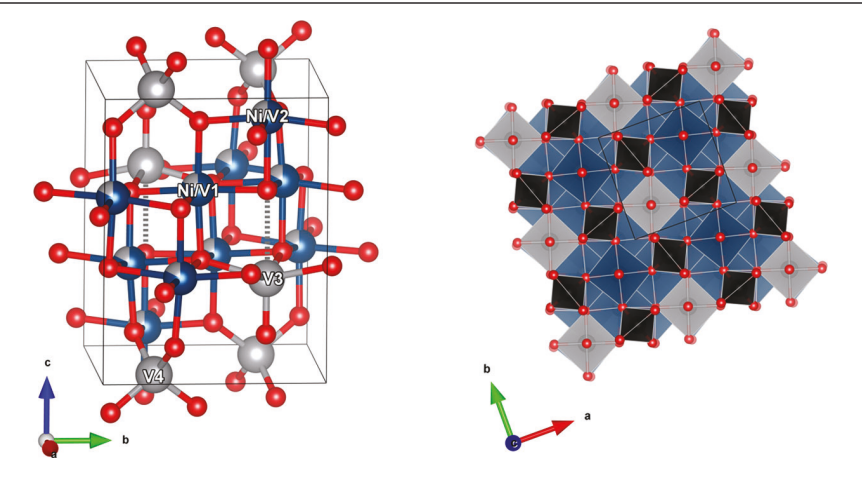


Figure 2. (Left) Unit cell of  $Ni_4V_3O_{10}$ . Ni ions are pictured in blue, V in gray, and O in red. Dashed lines are *trans* V–O bonds in the vanadyl octahedra. The structure contains three metal—oxygen coordination geometries: regular octahedra, tetrahedra, and vanadyl octahedra. (Right)  $2 \times 2 \times 1$  supercell of  $Ni_4V_3O_{10}$  viewed down the *c*-axis. Ni/V ions in regular octahedra are colored blue. V ions in vanadyl octahedra are gray. V ions in tetrahedra are black. O ions are red.

Table 1. Atomic Data for  $Ni_4V_3O_{10}$  (Refined to  $Ni_{3.995}V_{3.005}O_{10}$ ) from Co-refinement of 300 K POWGEN Powder Neutron Diffraction Data and 11-BM Powder X-ray Diffraction Data

atom	site	$\boldsymbol{x}$	у	z	$U_{\mathrm{iso}}\ (\mathrm{\AA}^2)$	occupancy
Ni1/V1	8 <i>g</i>	0.55160(5)	0.15332(5)	0.36493(3)	0.00311(4)	0.822/0.178(1)
Ni2/V2	2c	0.25	0.25	0.09935(8)	0.0052(1)	0.707/0.293(2)
V3	2 <i>c</i>	0.25	0.25	0.6659(1)	0.0040(2)	1
V4	2a	0.25	0.75	0	0.0033(2)	1
O1	8 <i>g</i>	0.0355(1)	0.65569(9)	0.38899(5)	0.00502(9)	1
O2	8 <i>g</i>	0.54980(7)	0.1770(1)	0.12310(7)	0.0062(1)	1
O3	2c	0.25	0.25	0.3552(2)	0.0059(2)	1
O4	2c	0.25	0.25	0.8614(2)	0.0088(2)	1
a = b = 6.478314(8) Å, $c = 8.35224(1)$ Å, Space Group $P4/n$ .						

in the Vienna Ab-initio Simulation Package (VASP). 26-28 To describe the exchange-correlation energy, the generalized gradient approximation (GGA) developed by Perdew, Burke, and Ernzerhof (PBE)<sup>29</sup> was used, and to account for electron correlations, the Hubbard U method<sup>30</sup> was applied. Similar to previous studies of other phases of the Ni–V–O system, such as NiV<sub>3</sub>O<sub>8</sub>, Ni<sub>3</sub>V<sub>2</sub>O<sub>8</sub>, Ni<sub>2</sub>V<sub>2</sub>O<sub>7</sub>, and NiVO<sub>3</sub>,  $^{31}$  the simplified rotationally invariant U - J on-site Coulomb interaction scheme developed by Dudarev et al.<sup>32</sup> was used with values of 6.2 eV for Ni d states and 3.2 eV for V d states. The projectoraugmented wave (PAW) scheme<sup>33</sup> was used to describe the electron-ion interaction. Based on the results of a convergence test, the single-particle wave functions were expanded into a plane-wave basis up to a cutoff energy of 600 eV, and the Brillouin zone was sampled by a  $\Gamma$ -centered  $9 \times 8 \times 8$  k-point mesh, allowing for the computation of total energies converged to within 1.65 meV/atom.

The aforementioned occupational Ni/V site disorder of the Ni<sub>4</sub>V<sub>3</sub>O<sub>10</sub> phase is challenging to model computationally because the periodic boundary conditions cannot be imposed in the same way as in perfect crystals. To simulate this material, the unit cell derived from the powder X-ray diffraction experiments, as shown in Figure 2, was the starting point. As listed in Table 1, two sites, Ni1/V1 and Ni2/V2, have site disorder with Ni as the sites' primary element. Based on Ni/V occupancy ratios of about 0.8:0.2 and 0.7:0.3 for Ni1/V1 and Ni2/V2 sites, respectively, and taking into account that the Ni1/V1 site includes 8 atoms while the Ni2/V2 site hosts 2 atoms, all possible configurations in which 8 of these doubly occupied sites are filled with Ni and 2 of them are filled with V were found. This is a simple combinatorial problem leading to  $\binom{10}{2}$  = 45 configurations, which reduce to 8 symmetrically distinct classes (see Table S134). For all of these, band structures, projected electronic densities of states, and dielectric functions<sup>28</sup> were computed and are discussed below.

### ■ RESULTS AND DISCUSSION

**Composition.** The crowded compositional space in which  $Ni_4V_3O_{10}$  sits makes it difficult to isolate the phase. In an effort to optimize the synthesis temperature, ball-milled samples were fired under vacuum at 700, 800, 850, 950, and 1050 °C. At 700 °C,  $V_{2-x}Ni_xO_3$  (45.2 wt %),  $Ni_3V_2O_8$  (33.6 wt %), and NiO (19.7 wt %) impurities dominated, and little  $Ni_4V_3O_{10}$  (1.5 wt %) was formed. At and above 850 °C,  $Ni_4V_3O_{10}$  was formed with NiO and  $V_{2-x}Ni_xO_3$  impurities that increased with temperature but without  $Ni_3V_2O_8$ . Firing at 800 °C under vacuum consistently provided the highest purity samples. When fired in air at 800 °C instead of under vacuum,

vanadium was fully oxidized to  $V^{5+}$ , and  $Ni_3V_2O_8$  was formed exclusively. Under Ar flow, only 5.7 wt % of the product was  $Ni_4V_3O_{10}$  (39.0 wt %  $Ni_3V_2O_8$ , 33.5 wt %  $V_{2-x}Ni_xO_3$ , 21.8 wt % NiO). Although NiVO<sub>3</sub> is closer on the phase diagram to  $Ni_4V_3O_{10}$  than  $V_{2-x}Ni_xO_3$ , it was not observed under any of these synthesis conditions. In the past, NiVO<sub>3</sub> has been produced only by high-pressure solid-state<sup>35</sup> and high-pressure hydrothermal<sup>13</sup> techniques.

According to Rietveld refinements of the X-ray diffraction data, the highest purity sample contained 89.5  $\pm$  0.3 wt %  $\mathrm{Ni_4V_3O_{10}}$  for the ball-milling technique and 86.8  $\pm$  0.1 wt %  $\mathrm{Ni_4V_3O_{10}}$  for the hand-grinding technique. Neutron powder diffraction data revealed that ball milling introduced an  $\mathrm{Fe_2O_3}$  impurity of about 0.03 wt % in the product. A small peak for this impurity could also be found in the 11-BM X-ray diffraction pattern at d=2.50 Å (Figure S1 $^{34}$ ). The other expected prominent structural peaks of  $\mathrm{Fe_2O_3}$  at d=2.69 and 3.67 Å overlap with peaks of other phases and thus were not distinguishable in the data. Qualitative XRF confirmed that Fe was present in ball-milled samples but absent in hand-ground samples. The  $\mathrm{Fe_2O_3}$  impurity comes from the oxidation of Fe introduced by the stainless steel balls during high-impact milling.

With co-refinement of 11-BM X-ray diffraction and POWGEN neutron diffraction data for a sample, the composition of the new ternary phase was refined to Ni<sub>3,995</sub>V<sub>3,005</sub>O<sub>10</sub> (Ni and V  $esd=\pm 0.002$ ). The co-refinement presented no evidence of oxygen vacancies. It is assumed here that the composition is Ni<sub>4</sub>V<sub>3</sub>O<sub>10</sub>. EDS point measurements corroborating this Ni/V ratio are presented in the Supporting Information. <sup>34</sup>

**Crystal Structure.** The crystal structure of  $\mathrm{Ni_4V_3O_{10}}$  was solved in the P4/n space group with powder X-ray diffraction data from a sample made by the ball-milling procedure. The unit cell of  $\mathrm{Ni_4V_3O_{10}}$  contains two formula units and is shown in Figure 2. The structure includes regular-octahedral, tetrahedral, and vanadyl-octahedral cation—oxygen coordination geometries. While nickel ions are present only on regular-octahedral sites, the vanadium ions occupy every cation site. The polyhedra form a set of three distorted planes normal to the c-axis, and the structure contains a checkerboard pattern resembling a rock-salt structure.

The subsequent co-refinement to X-ray and neutron powder diffraction data included the new phase (87.4 wt %),  $V_{2-x}Ni_xO_3$  (6.8 wt %), and NiO (5.8 wt %). The x value in  $V_{2-x}Ni_xO_3$  refined to 0.506(6), indicating the solid solution was below its reported solubility limit of x=0.75. The refinements and impurity-phase contributions are shown in Figure 3, and refined atomic parameters are reported in Table

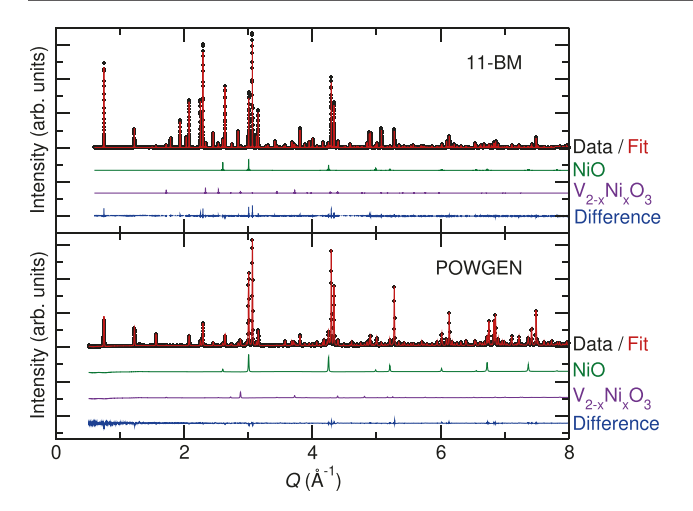


Figure 3. Rietveld co-refinement of synchrotron radiation powder X-ray diffraction (APS 11-BM) and time-of-flight powder neutron diffraction (ORNL POWGEN) data for a sample with 87.4 wt % Ni<sub>4</sub>V<sub>3</sub>O<sub>10</sub>.

1. The  $\mathrm{Fe_2O_3}$  impurity introduced by ball milling was not included due to its extremely small contribution to the structural peaks. Every peak reported by Gianoglio and Ramonda<sup>18</sup> was observed.

Two cation sites are occupationally disordered, with Ni as the sites' primary element. These cation sites form slightly distorted rock-salt-like edge-sharing octahedra with oxygen, here denoted as "regular octahedra." NiVO3, NiV3O8, and  $V_{2-x}Ni_xO_3$  also contain metal—oxygen octahedra but no other coordination geometries. Of these, only  $V_{2-x}Ni_xO_3$  involves occupational site disorder.

The other two metal sites in  $Ni_4V_3O_{10}$  are occupied exclusively by vanadium. One, V3, has a "vanadyl-octahedral" arrangement. The vanadyl octahedra consist of a 1.632(2) Å vanadyl bond (V=O), four 2.0012(7) Å equatorial bonds at a  $103.25(3)^{\circ}$  to the vanadyl bond, and a 2.595(2) Å *trans* bond, comfortably fitting the model of Schindler et al. <sup>36</sup> This coordination in  $Ni_4V_3O_{10}$  makes it unique among the Ni-V-O phases plotted in Figure 1. The second purely vanadium site, V4, is tetrahedrally coordinated to oxygen and is cornersharing with four Ni/V octahedra.

**Vanadium Oxidation States.** The coordination environments of the vanadium cations appear tied to their oxidation states. The V3 site's vanadyl bond and average vanadium to equatorial oxygen bond length of 2.00 Å identify it as exclusively  $V^{4+}$ . Bond valence sum (BVS) analysis indicates that the tetrahedrally coordinated vanadium ions (V4) have a +5 oxidation state. The difference value (bond valence sum minus nominal valence) is -0.011 assuming  $V^{5+}$  and +0.739 assuming  $V^{4+}$ . Similarly,  $V^{5+}$  cations in  $Ni_2V_2O_7$ ,  $Ni_3V_2O_8$ , and

NiV<sub>2</sub>O<sub>6</sub> exclusively form vanadium-oxygen tetrahedra. According to a statistical analysis of experimentally realized oxides by Waroquiers et al., tetrahedral coordination for V5+ is the most likely geometry (67.3%) and is unlikely for  $V^{4+}$  (4.99%) and  $V^{3+}$  (1.01%).<sup>37</sup> The V–O bond lengths in the tetrahedra are all 1.7213(6) Å. This value fits within the expected 1.6–2.0 Å range<sup>36</sup> and matches the average of 1.72(1) Å for tetrahedral V<sup>5+</sup>-O.<sup>38</sup> These factors give strong evidence for V4 being V5+. The presence of V5+ on this site would necessitate V3+ within the material on the mixed Ni/V regular-octahedral sites for charge balance because of the tight restriction on the composition seen in the diffraction corefinement result. BVS analysis of mixed occupancy sites can prove difficult, but Bosi demonstrates a technique where, in this case, the BVS values obtained assuming a purely nickel or vanadium site are averaged while weighting by site occupancy. This method can only give an indication of fit because of the valence sum rule assumption of regular, unstrained bonding and because of systematic error that increases as the site fractions of the cations approach 0.5.39 BVS results for this proposed three-state model are summarized in Table 2.

Other models can be explored with the BVS analysis. One option is to reduce the BVS difference value for V3, which has the largest difference of the four cation sites. Using Bosi's procedure with the two Ni/V sites produces a predicted oxidation state of V³+ for V1 (difference of -0.122) and V³+ (+0.093) or V⁴+ for V2 (-0.103). Both sites being +3 matches the bonding arguments, but if V2 is +4 and V4 is +5, then to have charge balance, V3 would require an average oxidation state of +3.726, resulting in a lower difference of +0.005, but this model ignores strong bonding evidence for V3 and offers no descriptive advantage, still resulting in three oxidation states

Since there is a chance, though small, that the tetrahedral site is  $V^{4+}$ , for completeness, if instead, one assumes that every vanadium ion has an oxidation state of +4, the average expected from the nominal chemical formula, the results produce significantly higher difference values for the Ni1/V1 (-0.336) and V4 (+0.739) sites than with the bonding-derived three-state model. This single-state model, therefore, increases BVS differences while also ignoring the strong arguments for tetrahedral  $V^{5+}$ .

XPS spectra for a  $Ni_4V_3O_{10}$  sample and the  $V_2O_5$  powder used for synthesis are shown in Figure 4. Even after binding energy referencing to the C 1s peak, the  $V_2O_5$  O 1s peak is +0.53 eV from its expected position at 530.0 eV, and the V  $2p_{3/2}$  peak is +0.51 eV from its expected 517.2 eV. <sup>40,41</sup> This consistent shift, though, does not prevent the analysis of vanadium oxidation states since it has been shown that despite shifts in O 1s position, the energy difference between the O 1s and V  $2p_{3/2}$  peaks is a reliable measure of oxidation state.

Table 2. Bond Valence Sum Analysis Fits for Ni<sub>4</sub>V<sub>3</sub>O<sub>10</sub> When Following Techniques for Mixed Sites Proposed by Bosi<sup>39</sup>

site	oxygen coordination	nominal V valence	weighted site valence	$R_0^{a}$	BVS	difference
Ni1/V1	regular-octahedral	+3	+2.178	1.654 (Ni <sup>2+</sup> ), 1.743 (V <sup>3+</sup> )	2.056	-0.122
Ni2/V2	regular-octahedral	+3	+2.293	1.654 (Ni <sup>2+</sup> ), 1.743 (V <sup>3+</sup> )	2.386	+0.093
V3	vanadyl-octahedral	+4	+4	$1.784 (V^{4+})$	3.842	-0.158
V4	tetrahedral	+5	+5	1.803 (V <sup>5+</sup> )	4.989	-0.011

<sup>&</sup>lt;sup>a</sup>Values from Brown and Altermatt.<sup>24</sup>

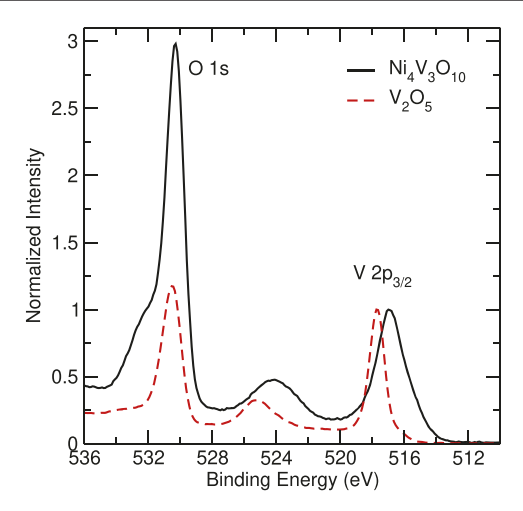


**Figure 4.** XPS spectra of the O 1s and V  $2p_{3/2}$  peaks for Ni<sub>4</sub>V<sub>3</sub>O<sub>10</sub> and V<sub>2</sub>O<sub>5</sub> (99.6%, as received). The Ni<sub>4</sub>V<sub>3</sub>O<sub>10</sub> spectrum indicates the presence of V<sup>4+</sup> as well as an oxide/hydroxide surface layer.

Expected shifts of binary vanadium oxides are  $\sim$ 12.80 eV for  $V_2O_5$ ,  $\sim$ 13.45 eV for  $VO_2$ , and  $\sim$ 14.50 eV for  $V_2O_3$ .<sup>40</sup> For the  $V_2O_5$  reference, this difference is 12.82 eV; for  $Ni_4V_3O_{10}$ , it is 13.42 eV. Along with the expected increase in  $V_2O_{3/2}$  peak width from  $V_3^{5+}$  to  $V_3^{4+}$ , this peak position difference for  $V_3^{5+}$ 0 indicates the presence of  $V_3^{5+}$ 0.

The presence of an additional shoulder in the O 1s peak of  $\mathrm{Ni_4V_3O_{10}}$  also reveals moisture contamination on the surface. This effect has been noted in samples of  $\mathrm{V_2O_5}^{41}$  vanadium—yttrium hydrates, and NiO. This oxide/hydroxide layer likely protects the vanadium near the surface of  $\mathrm{Ni_4V_3O_{10}}$  from oxidizing to  $\mathrm{V^{5+}}$  in air. This data, though, cannot reveal the presence of multiple oxidation states within the bulk of the material, as XPS is a surface probing technique.

To try to probe the bulk, a STEM-EELS spectrum was collected for a  $\rm Ni_4V_3O_{10}$  grain oriented down the [001] direction but did not provide additional insights into the oxidation states of  $\rm Ni_4V_3O_{10}$  (see the Supporting Information  $^{34}$ ). Consequently, three oxidation states are assigned to the vanadium sites using bonding arguments for tetrahedral  $\rm V^{5+}$  and vanadyl-octahedral  $\rm V^{4+}$ , the subsequent requirement of  $\rm V^{3+}$  for charge balance, and the broad V  $\rm 2p_{3/2}$  XPS peak suggesting  $\rm V^{4+}$  in the material.

Although oxides containing cations exhibiting three oxidation states are rare, they have similarities to Ni<sub>4</sub>V<sub>3</sub>O<sub>10</sub>. The multiple state cations, in most cases, occupy multiple coordination environments in the structures, 45-53 with the only exception being Mn in the perovskite (La,Ca,K)-MnO<sub>3</sub>. 54,55 Notably, Ba<sub>15</sub>V<sub>12</sub>S<sub>34</sub>O<sub>3</sub> contains V<sup>3+</sup> on octahedral sites, V4+ on a site distorted between vanadyl-octahedral ("V1a") and octahedral ("V1b") coordination, and V5+ on a tetrahedral site.<sup>53</sup> These coordination structures match the behavior of  $\mathrm{Ni_4V_3O_{10}}$  well. Also deserving special attention are Ni<sub>x</sub>Mn<sub>3-x</sub>O<sub>4</sub><sup>47<sup>4</sup></sup> and Cu<sub>x</sub>Mn<sub>3-x</sub>O<sub>4</sub>, two occupationally disordered spinels, a structure type containing octahedral and tetrahedral coordination geometries. In both, the tetrahedral sites are Mn<sup>2+</sup> and the octahedral sites are mixed Mn<sup>3+/4+</sup>. In the same way, H<sub>x</sub>Li<sub>y</sub>Co<sub>3-δ</sub>O<sub>4</sub> (typically near H<sub>0.37</sub>Li<sub>0.16</sub>Co<sub>2.66</sub>O<sub>4</sub>) forms a spinel structure with Co<sup>2+</sup> in the tetrahedral sites and with Co3+ and Co4+ on the octahedral sites. Li substitution into the base Co<sub>3</sub>O<sub>4</sub> structure promotes the presence of Co4+ 49,56-58 These three compounds demonstrate how occupational disorder can promote the coexistence of three cation oxidation states.

Absorption Properties and Band Character. UV–vis spectroscopy reflectance data was transformed using the Kubelka–Munk theory<sup>59</sup> to give the absorption spectrum of  $Ni_4V_3O_{10}$ . A Tauc plot for modeling direct band gaps<sup>60</sup> was then constructed to observe the gap (Figure 5). Following the

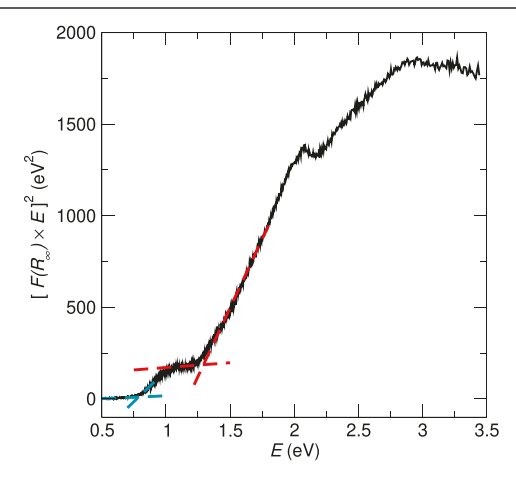
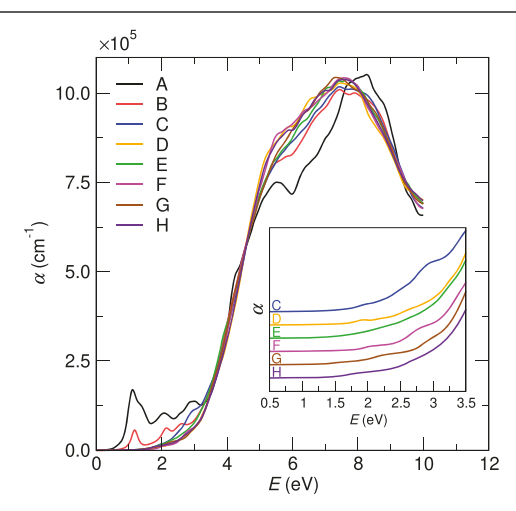


Figure 5. Tauc plot showing intersecting dashed lines at the onsets associated with direct band gaps.

procedure of Makuła et al., the intersection of regression lines was used to determine the band gap associated with an onset in the Tauc plot. <sup>61</sup> Two onsets were observed, one at 0.79 eV and another at 1.29 eV.

Absorption coefficients computed using DFT + U for the eight permutations of Ni/V ordered classes are shown in Figure 6. Classes A and B show a peak structure in the <4 eV



**Figure 6.** Calculated absorption coefficients,  $\alpha$ , for the eight classes. Classes A and B show a noticeable peak structure in the <4 eV region. The inset shows the more featureless shape of the other six classes at low energy, with the values of  $\alpha$  offset uniformly for each.

energy region, while classes C–H show steps in this energy range. While classes A and B have a non-zero absorption coefficient at energy values less than 1 eV, the others do not until around 1.5 eV. The densities of states for each class (see the Supporting Information<sup>34</sup>) reveal that the differences in classes A and B arise from an additional V d orbital in the

valence band. This additional orbital would be consistent with the inclusion of  $V^{3+}$   $3d^2$  states that are necessary to balance the  $V^{5+}$  that is clearly evident in bond valence analysis. This difference also manifests itself in the calculated band gaps in Table 3, where the "gap 1" values (associated with spin component 1) are significantly smaller for classes A and B. Band structure plots are also available in the Supporting Information.<sup>34</sup>

Table 3. Calculated Band Gaps for the Eight Classes along with Their Relative Calculated Energies $^a$ 

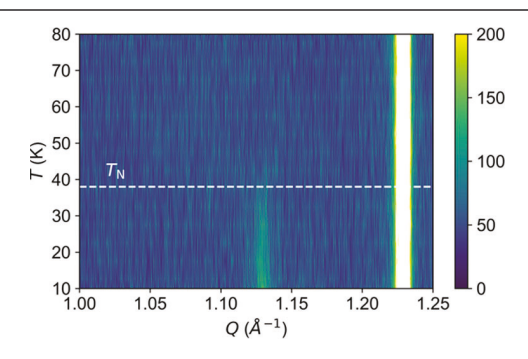
class	gap 1 (eV)	gap 2 (eV)	relative total energy (meV/atom)
A	0.54	3.21	+45.7
В	0.68	3.00	+25.6
C	1.33	2.92	<u>±</u> 0
D	1.76	3.36	+5.07
E	1.31	2.95	+51.5
F	1.90	3.12	+38.5
G	1.42	2.82	+12.0
Н	1.54	3.09	+7.64

 $^{a}$ Gap 1 (2) corresponds to the smallest band gap for spin component 1 (2).

**Magnetic Properties.** *Magnetometry Data.* The magnetic properties of  $Ni_4V_3O_{10}$  were explored with a sample produced by the hand-grinding method to eliminate the contribution of any  $Fe_2O_3$  impurity. The field cooled (FC) and zero-field cooled (ZFC) susceptibility curves were measured between 2 and 400 K and are shown in Figure 7, and isothermal magnetization data are presented in Figure S7. The most frequent impurity in  $Ni_4V_3O_{10}$  samples,  $V_{2-x}Ni_xO_3$ , is a ferromagnet with an unreported magnetic structure. It has a Curie temperature of 142 K and an additional transition, here denoted  $T^*$ , at 56 K. The FC curve for this impurity is shown in Figure S8. The Since a sharp increase in susceptibility at  $T_C$  occurs in any sample with a  $V_{2-x}Ni_xO_3$  impurity, we can be sure that the data in Figure 7 is from  $Ni_4V_3O_{10}$  alone. The bifurcation of the FC and ZFC curves in Figure 7 suggests a

Néel temperature  $T_{\rm N}$  = 38 K, confirmed by neutron diffraction data.

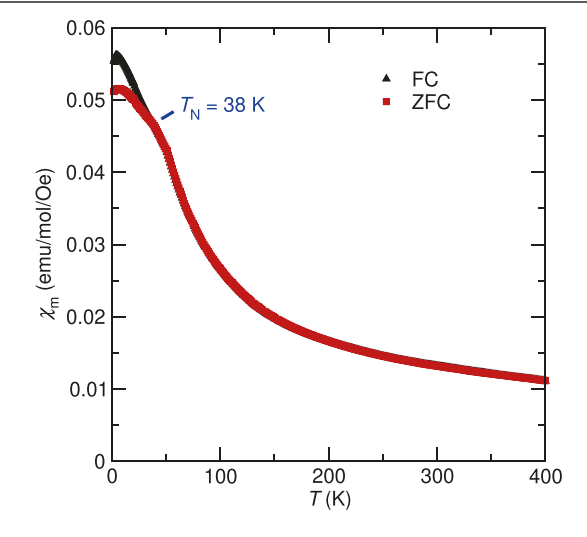
Neutron Diffraction Data. In addition to magnetometry data, POWGEN neutron powder diffraction data collected while cooling from 80 K to around 9 K confirms this transition. A significant magnetic peak that appears at d = 5.57 Å indicates that the transition at 38 K corresponds to Ni<sub>4</sub>V<sub>3</sub>O<sub>10</sub>. The onset of this peak can be observed using a contour plot constructed with 5 K diffraction data bins (Figure 8). Its intensity relative



**Figure 8.** Contour plot using 5 K splits of ramping data. The new magnetic peak at Q=1.13 Å $^{-1}$  (d=5.57 Å) is shown along with the structural peak at Q=1.23 Å $^{-1}$  (d=5.11 Å). The scale used improves the visibility of the magnetic peak, but it also tops off the structural peak's maximum intensity of around 800 (arbitrary units). The magnetic peak clearly appears below  $T_{\rm N}$ .

to the background is plotted in Figure S9.<sup>34</sup> Additional low-intensity peaks are apparent in the long isothermal neutron powder diffraction collection at 6.4 K at d=10.40, 10.06, 5.57, 5.39, 3.97, 2.88, and 2.36 Å. These peaks are tentatively assigned to Ni<sub>4</sub>V<sub>3</sub>O<sub>10</sub> and are plotted in Figure 9.

By exploring the maximal magnetic space groups for the P4/n crystallographic space group, it is clear that the magnetic structure of  $Ni_4V_3O_{10}$  is not a simple commensurate phase with a magnetic propagation vector of  $\mathbf{k} = \mathbf{0}$ . There are six maximal space groups: P4/n and P2'/c' can be ruled out due to their ferromagnetic ordering, while P4'/n and P4'/n' do not



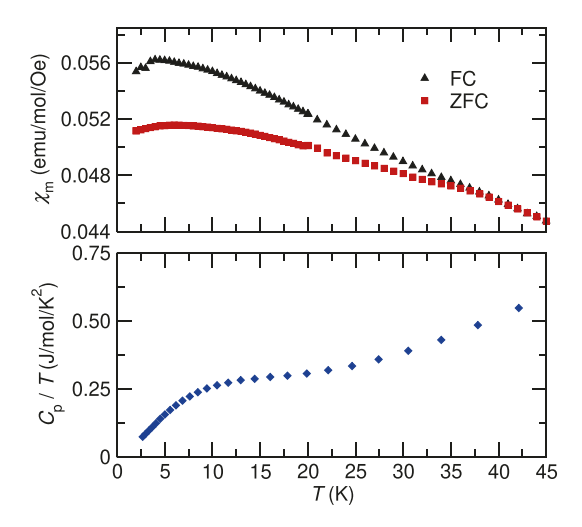


Figure 7. (Left) Field cooling and zero field cooling molar susceptibility collected from 2–400 K at 1000 Oe for a  $Ni_4V_3O_{10}$  sample. The Néel temperature for  $Ni_4V_3O_{10}$  manifests as the split between the curves at 38 K. (Right) Low-temperature FC and ZFC data paired with the temperature-normalized heat capacity of  $Ni_4V_3O_{10}$  from 2–45 K. The broad hump centered below  $T_N$  in the heat capacity data has been noted in other materials with magnetic frustration,  $^{62,63}$  site disorder,  $^{64}$  and complex coordination and oxidation chemistry.  $^{53}$ 

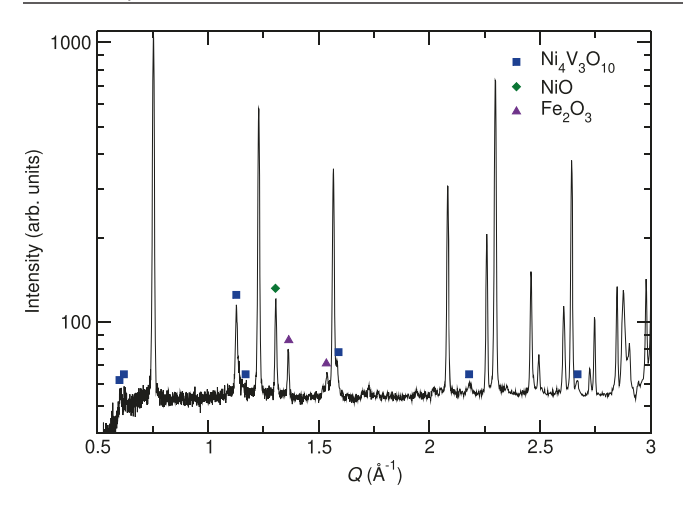


Figure 9. Peaks in the 6.4 K neutron powder diffraction data that are not present at room temperature are marked with squares. NiO and Fe<sub>2</sub>O<sub>3</sub> impurity magnetic peaks that are present at 6.4 K and room temperature are marked as well. All unmarked peaks are structural.

allow local moments on the Ni2/V2 or V3 sites. To visualize the remaining two, magnetic moments with arbitrary and equal magnitudes are assigned to each space group based on the allowed moment directions. The first magnetic space group, P4/n', allows for a, b, and c components of the moment on Ni1/V1 and for only a c component on Ni2/V2 and V3. The other, P2'/c, splits Ni1/V1 into two magnetic symmetry sites, each with a possible a, b, and c component to the magnetic

moment, but unlike with P4/n', Ni2/V2, and V3 magnetic moments are restricted to the ab-plane.

However, antiferromagnetic ordering is violated for both P4/n' and P2'/c in Ni<sub>4</sub>V<sub>3</sub>O<sub>10</sub> through Ni<sub>2</sub>/V2-O-V3 bonding paths between cells along the c-axis and also through Ni1/V1-O-Ni1/V1 bonding paths within the crystallographic cell. Figure 10a shows the spin arrangement of P4/n', and Figure 10b shows that of P2'/c. Oxide ions are omitted for clarity of the spin orientations. Figure 10a includes an additional Ni2/ V2 ion from the cell above and a V3 ion from the cell below. The polyhedral connections between these ions (opaque polyhedra in Figure 10c) demonstrate how these connections break antiferromagnetic ordering across 180° superexchange paths. Moreover, Figure 10b includes a (001) slice in the cell to illustrate the other discrepancy's location. In this slice, the opaque polyhedra in Figure 10d have the same spin orientations and violate antiferromagnetic ordering. Both P4/ n' and P2'/c contain both spin orientation issues.

These arguments explain why  $\mathbf{k}=\mathbf{0}$  ordering is not adopted in Ni<sub>4</sub>V<sub>3</sub>O<sub>10</sub>. The magnetic peak assigned to Ni<sub>4</sub>V<sub>3</sub>O<sub>10</sub> at d=5.57 Å could be indexed as (003) under the assumption of caxis doubling, resulting in a magnetic propagation vector  $\mathbf{k}=\left(0,\,0,\,\frac{1}{2}\right)$ , but this assumption also produces structures incompatible with antiferromagnetic ordering and does not index the remaining neutron diffraction peaks.

Frustrated Magnetism in  $Ni_4V_3O_{10}$ . Having established that  $Ni_4V_3O_{10}$  has a Néel temperature of 38 K and does not experience  $\mathbf{k} = \mathbf{0}$  ordering, it is worth further exploring its

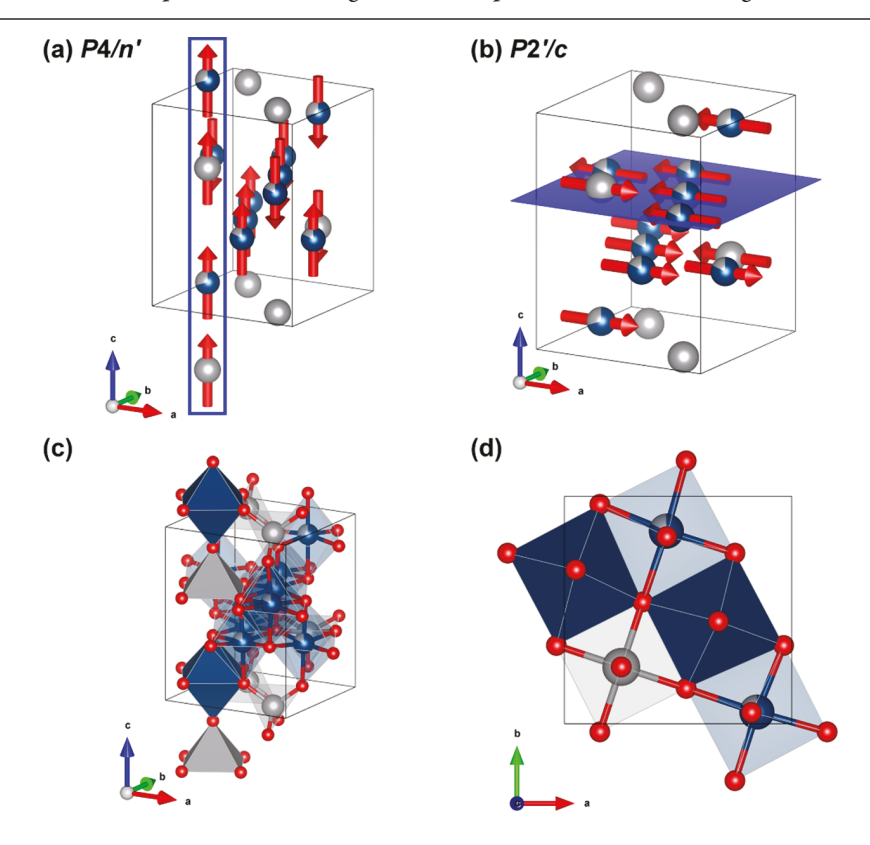
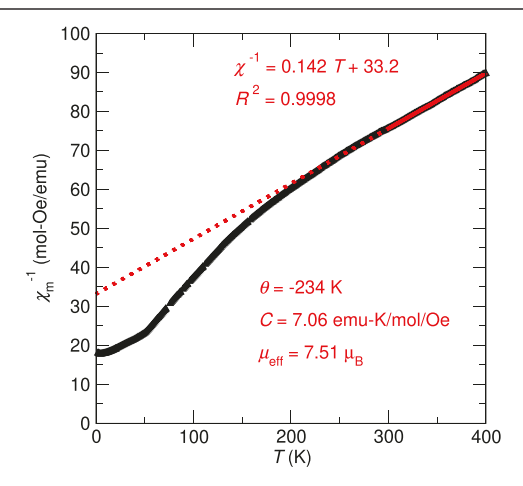


Figure 10. Two k = 0 maximal magnetic space groups for  $Ni_4V_3O_{10}$  with antiparallel moment arrangements on the Ni1/V1, Ni2/V2, and V3 sites. Panel (a) shows a P4/n' unit cell with a box enclosing the four inline ions that violate antiferromagnetic ordering. Panel (b) shows a P2'/c unit cell with a (001) plane. In panel (c), the Ni2/V2-O-V3 bonding path is presented with opaque polyhedra, and in panel (d), the Ni1/V1-O-Ni1/V1 path is presented with opaque polyhedra. These bonding structures paired with the ions' local moments violate antiferromagnetic ordering. Each space group contains both coordination violations.

nontrivial magnetic properties. A Curie-Weiss fit to magnetometry data above 300 K, shown in Figure 11, results in a



**Figure 11.** Curie—Weiss fit to 1000 Oe field cooling data above 300 K for  $Ni_4V_3O_{10}$ .

Curie–Weiss parameter  $\theta=-234$  K. Combined with the information about  $T_{\rm N}$  from the low-temperature magnetometry and neutron diffraction data, this indicates frustrated antiferromagnetic ordering with a frustration index of 6.2.

Additionally, low-temperature heat capacity measurements on Ni<sub>4</sub>V<sub>3</sub>O<sub>10</sub> show a broad peak below 30 K. As can be seen in Figure 7, this does not correspond to a change in the susceptibility curves. A similar heat capacity response has been noted in several spinel systems where mixed or frustrated magnetic behavior is present. For CoAl2O4 spinels, Tristan et al. show that with low substitution of Co onto the primarily Al octahedral site, a hump in the heat capacity appears slightly above the characteristic temperature, but with a greater degree of substitution, the hump broadens and appears at a lower temperature than the bifurcation in the FC and ZFC susceptibility curves.<sup>63</sup> They associate this behavior with a mixed magnetic phase. Ghara et al. likewise observe that increasing cation antisite disorder in CoAl2O4 samples shifts the heat capacity magnetic peak to lower temperatures and broadens it. 64 Another spinel system, FeSc<sub>2</sub>S<sub>4</sub>, also shows a broad peak below its ordering temperature that is associated with geometric magnetic frustration<sup>62</sup> and disorder in the sample. 65 Ba<sub>15</sub>V<sub>12</sub>S<sub>34</sub>O<sub>3</sub>, noted before for its structural similarities to  $Ni_4V_3O_{10}$  and its inclusion of  $V^{3+}$ ,  $V^{4+}$ , and V<sup>5+</sup> cations, similarly exhibits antiferromagnetic interactions and a broad hump in its  $C_p/T$  curve below the bifurcation of the FC and ZFC curves. Therefore, frustrated magnetic behavior in Ni<sub>4</sub>V<sub>3</sub>O<sub>10</sub> appears to lead to weak, incommensurate ordering that emerges over a range of temperatures below  $T_N$ . Single crystals may be needed to further explore the magnetic structure.

#### CONCLUSIONS

The crystal structure and antiferromagnetism of  $Ni_4V_3O_{10}$  have been presented. Two methods of powder preparation were used to form the structure at 800 °C. Although it requires much less time to achieve the same level of  $Ni_4V_3O_{10}$  content, the ball-milling method results in a small  $Fe_2O_3$  impurity that can affect magnetic characterization. The material is distinct from others in the Ni-V-O system in its inclusion of three metal—oxygen coordination structures, and the potential

presence of three vanadium oxidation states, which is ambiguous by XPS or STEM-EELS but is compatible with bonding analysis and neutron/X-ray co-refinement, would place it in a small class of oxides. DFT + U calculations for representatives of the eight symmetrically distinct classes show varying absorption coefficient and band gap behavior due to the presence or absence of an additional  $V^{3+}$   $3d^2$  orbital in the valence band. The structure's complexity, the emergence of low-intensity magnetic peaks, and the presence of  $V_{2-x}Ni_xO_3$ , a ferromagnetic material with an unsolved magnetic structure, prevented the solution of the magnetic structure of Ni<sub>4</sub>V<sub>3</sub>O<sub>10</sub> from a powder sample, although  $\mathbf{k} = \mathbf{0}$  and  $\mathbf{k} = (0, 0, \frac{1}{2})$ magnetic structures were ruled out. Still, magnetometry, neutron powder diffraction data, and heat capacity measurements showed that Ni<sub>4</sub>V<sub>3</sub>O<sub>10</sub> is antiferromagnetic ( $T_N = 38 \text{ K}$ ) with strong geometric frustration arising from staggered rocksalt-like motifs. Further study into single-crystal growth of the material could lead to the solution of the material's magnetic structure, could provide data for understanding the variability of the Ni/V site mixing, and could allow for a more precise determination of the vanadium oxidation state distribution.

#### ASSOCIATED CONTENT

## Supporting Information

The Supporting Information is available free of charge at https://pubs.acs.org/doi/10.1021/acs.chemmater.2c00697.

Fe $_2$ O $_3$  impurity peak in neutron diffraction data (Figure S1); SEM image of sample used for EDS point measurements (Figure S2); DFT simulation cell configurations (Table S1); DFT + U total energy results (Table S2); DFT simulation cell (Figure S3); DFT + U calculated band structures (Figure S4); DFT + U projected densities of states (Figure S5). STEM-EELS spectrum for a grain of Ni $_4$ V $_3$ O $_{10}$  (Figure S6); Isothermal magnetization data for Ni $_4$ V $_3$ O $_{10}$  (Figure S7); Field cooling susceptibility curve of V $_{2-x}$ Ni $_x$ O $_3$  (Figure S8); and Ni $_4$ V $_3$ O $_{10}$  magnetic peak intensity relative to background intensity (Figure S9) (PDF) Crystallographic data (CIF)

## AUTHOR INFORMATION

#### **Corresponding Author**

Daniel P. Shoemaker — Department of Materials Science and Engineering, University of Illinois at Urbana-Champaign, Urbana, Illinois 61801, United States; Materials Research Laboratory, University of Illinois at Urbana-Champaign, Urbana, Illinois 61801, United States; ◎ orcid.org/0000-0003-3650-7551; Email: dpshoema@illinois.edu

#### **Authors**

Zachary W. Riedel — Department of Materials Science and Engineering, University of Illinois at Urbana-Champaign, Urbana, Illinois 61801, United States; Materials Research Laboratory, University of Illinois at Urbana-Champaign, Urbana, Illinois 61801, United States; orcid.org/0000-0001-5848-5520

Fatemeh Amerikheirabadi — Department of Physics and Materials Research Laboratory, University of Illinois at Urbana-Champaign, Urbana, Illinois 61801, United States Kejian Qu — Department of Physics and Materials Research Laboratory, University of Illinois at Urbana-Champaign,

- Urbana, Illinois 61801, United States; o orcid.org/0000-0002-7189-537X
- Jeffrey Huang Department of Materials Science and Engineering, University of Illinois at Urbana-Champaign, Urbana, Illinois 61801, United States; Materials Research Laboratory, University of Illinois at Urbana-Champaign, Urbana, Illinois 61801, United States; Occid.org/0000-0002-5055-1666
- Mebatsion S. Gebre Department of Materials Science and Engineering, University of Illinois at Urbana-Champaign, Urbana, Illinois 61801, United States; Materials Research Laboratory, University of Illinois at Urbana-Champaign, Urbana, Illinois 61801, United States; orcid.org/0000-0002-8980-6507
- Ankita Bhutani Department of Materials Science and Engineering, University of Illinois at Urbana-Champaign, Urbana, Illinois 61801, United States; Materials Research Laboratory, University of Illinois at Urbana-Champaign, Urbana, Illinois 61801, United States; orcid.org/0000-0001-8053-5432
- Richard T. Haasch Materials Research Laboratory, University of Illinois at Urbana-Champaign, Urbana, Illinois 61801, United States; o orcid.org/0000-0001-9479-2595
- Pinshane Y. Huang Department of Materials Science and Engineering, University of Illinois at Urbana-Champaign, Urbana, Illinois 61801, United States; Materials Research Laboratory, University of Illinois at Urbana-Champaign, Urbana, Illinois 61801, United States; orcid.org/0000-0002-1095-1833
- André Schleife Department of Materials Science and Engineering, University of Illinois at Urbana-Champaign, Urbana, Illinois 61801, United States; Materials Research Laboratory and National Center for Supercomputing Applications, University of Illinois at Urbana-Champaign, Urbana, Illinois 61801, United States; orcid.org/0000-0003-0496-8214

Complete contact information is available at: https://pubs.acs.org/10.1021/acs.chemmater.2c00697

#### Notes

The authors declare no competing financial interest.

### ACKNOWLEDGMENTS

The authors thank Maxim Avdeev for his helpful input on the viability of solving the magnetic structure with the current set of neutron diffraction data. Synthesis and characterization were supported by the U.S. Department of Energy (DOE), Basic Energy Sciences (Grant No. DE-SC0013897) for Early Career Research and were carried out in part at the Materials Research Laboratory (MRL) Central Research Facilities, University of Illinois. The STEM experiments were likewise carried out at the MRL Central Research Facilities and were supported by the Air Force Office of Scientific Research under Award FA9550-20-1-0302 and by the National Science Foundation under Grant No. 1922758. Computational work was supported by Illinois MRSEC, NSF Award No. DMR-1720633; this work made use of the Illinois Campus Cluster, a computing resource that is operated by the Illinois Campus Cluster Program (ICCP) in conjunction with the National Center for Supercomputing Applications (NCSA) and which is supported by funds from the University of Illinois at Urbana-Champaign. Neutron scattering was performed at the Spallation Neutron

Source, a DOE Office of Science User Facility operated by the Oak Ridge National Laboratory. Use of synchrotron X-ray powder diffraction at beamline 11-BM of the Advanced Photon Source at Argonne National Laboratory was supported by the U.S. Department of Energy, Office of Science, Office of Basic Energy Sciences, under Contract No. DE-AC02-06CH11357.

#### REFERENCES

- (1) He, Z.; Ueda, Y.; Itoh, M. Crystal growth of Ni<sub>3</sub>V<sub>2</sub>O<sub>8</sub> by flux method. *J. Cryst. Growth* **2006**, 297, 1–3.
- (2) Rogado, N.; Lawes, G.; Huse, D. A.; Ramirez, A.; Cava, R. J. The Kagomé-staircase lattice: magnetic ordering in  $Ni_3V_2O_8$  and  $Co_3V_2O_8$ . Solid State Commun. **2002**, 124, 229–233.
- (3) Hosseini, H.; Shahrokhian, S. Advanced binder-free electrode based on core—shell nanostructures of mesoporous  $\text{Co}_3\text{V}_2\text{O}_8$ - $\text{Ni}_3\text{V}_2\text{O}_8$  thin layers@porous carbon nanofibers for high-performance and flexible all-solid-state supercapacitors. *Chem. Eng. J.* **2018**, 341,  $10{-}26$ .
- (4) Huang, Y.; Feng, X.; Li, C.; Li, Y.; Chen, X.; Gao, X.; Chen, C.; Guang, Z.; Liu, P. Construction of hydrangea-like ZnCo<sub>2</sub>O<sub>4</sub>/Ni<sub>3</sub>V<sub>2</sub>O<sub>8</sub> hierarchical nanostructures for asymmetric all-solid-state supercapacitors. *Ceramics International* **2019**, *45*, 15451–15457.
- (5) Liu, X.; Wang, J.; Yang, G. In situ growth of the Ni<sub>3</sub>V<sub>2</sub>O<sub>8</sub>@PANI composite electrode for flexible and transparent symmetric supercapacitors. ACS Appl. Mater. Interfaces 2018, 10, 20688–20695.
- (6) Vishnukumar, P.; Saravanakumar, B.; Ravi, G.; Ganesh, V.; Guduru, R. K.; Yuvakkumar, R. Synthesis and characterization of NiO/Ni $_3$ V $_2$ O $_8$  nanocomposite for supercapacitor applications. *Mater. Lett.* **2018**, 219, 114–118.
- (7) Rozier, P.; Combes, M.; Galy, J. NiV<sub>3</sub>O<sub>8</sub> single crystal structure determination and comparison with polymorphic forms of ZnV<sub>3</sub>O<sub>8</sub> and MgV<sub>3</sub>O<sub>8</sub>. *J. Phys. Chem. Solids* **2001**, *62*, 1401–1408.
- (8) He, Z.; Yamaura, J.-I.; Ueda, Y.; Cheng, W. Crystal growth and multiple magnetic transitions of the spin-1 chain system  $Ni_2V_2O_7$ . *Phys. Rev. B: Condens. Matter Mater. Phys.* **2009**, 79, No. 092404.
- (9) Baba Ali, E.; Bernede, J.; Guyomard, D. Ni<sub>2</sub>V<sub>2</sub>O<sub>7</sub> thin films for negative electrode application of rechargeable microbatteries. *Thin Solid Films* **2002**, 402, 215–221.
- (10) Cui, P.; Liang, Y.; Zhan, D.; Zhao, Y. Synthesis and characterization of NiV<sub>3</sub>O<sub>8</sub> powder as cathode material for lithiumion batteries. *Electrochim. Acta* **2014**, *148*, 261–265.
- (11) Ni, S.; Ma, J.; Lv, X.; Yang, X.; Zhang, L. The preparation of  $NiV_3O_8/Ni$  composite *via* an *in situ* corrosion method and its use as a new sort of anode material for Li-ion batteries. *J. Mater. Chem. A* **2014**, 2, 8995–8998.
- (12) Ni, S.; Ma, J.; Zhang, J.; Yang, X.; Zhang, L. Excellent electrochemical performance of NiV<sub>3</sub>O<sub>8</sub>/natural graphite anodes *via* novel *in situ* electrochemical reconstruction. *Chem. Commun.* **2015**, 51, 5880–5882.
- (13) McNulty, D.; Collins, G.; O'Dwyer, C. NiVO<sub>3</sub> fused oxide nanoparticles—an electrochemically stable intercalation anode material for lithium ion batteries. *J. Mater. Chem. A* **2018**, *6*, 18103—18115.
- (14) Zhou, Z.; Zhang, J.; Chen, S.; Yao, H.; Zhao, Y.; Kuang, Q.; Fan, Q.; Dong, Y. The electrochemical performance and multielectron reaction mechanism of  $NiV_2O_6$  as a novel anode material for lithiumion batteries. *Electrochim. Acta* **2020**, 359, No. 136979.
- (15) Li, Y.; Sun, H.; Yang, Y.; Cao, Y.; Zhou, W.; Chai, H. Controllable fabrication of  $\mathrm{NiV_2O_6}$  nanosphere as a high-performance flexible all-solid-state electrode material for supercapacitors. *J. Colloid Interface Sci.* **2020**, 580, 298–307.
- (16) Bouloux, J.-C.; Milosevic, I.; Sénégas, J. Étude structurale et magnétique comparative des solutions solides  $M_x^{2+}V_x^{4+}V_{2-2x}^{3+}O3$  (M= Mg, Ni). Revue de Chimie Minérale 1974, 11, 701–709.
- (17) Rozier, P.; Ratuszna, A.; Galy, J. Comparative Structural and Electrical Studies of  $V_2O_3$  and  $V_{2-x}Ni_xO_3$  (0 < x < 0.75) Solid Solution. Z. Anorg. Allg. Chem. **2002**, 628, 1236–1242.
- (18) Gianoglio, C.; Ramonda, G. Recherches sur le Système Nickel-Vanadium-Oxygène. Rev. int. Htes Temp. et Réfract. 1973, 10, 27–30.

- (19) Favre-Nicolin, V.; Černý, R. FOX, 'free objects for crystallography': a modular approach to ab initio structure determination from powder diffraction. *J. Appl. Crystallogr.* **2002**, 35, 734–743.
- (20) Toby, B. H.; Von Dreele, R. B. GSAS-II: the genesis of a modern open-source all purpose crystallography software package. *J. Appl. Crystallogr.* **2013**, *46*, 544–549.
- (21) Capillas, C.; Tasci, E. S.; de la Flor, G.; Orobengoa, D.; Perez-Mato, J. M.; Aroyo, M. I. A new computer tool at the Bilbao Crystallographic Server to detect and characterize pseudosymmetry. *Z. Kristallogr. Cryst. Mater.* **2011**, 226, 186–196.
- (22) Perez-Mato, J.; Gallego, S.; Tasci, E.; Elcoro, L.; de la Flor, G.; Aroyo, M. Symmetry-based computational tools for magnetic crystallography. *Annu. Rev. Mater. Res.* **2015**, *45*, 217–248.
- (23) Momma, K.; Izumi, F. VESTA 3 for three-dimensional visualization of crystal, volumetric and morphology data. *J. Appl. Crystallogr.* **2011**, *44*, 1272–1276.
- (24) Brown, I. D.; Altermatt, D. Bond-valence parameters obtained from a systematic analysis of the inorganic crystal structure database. *Acta Crystallogr., Sect. B: Struct. Sci.* **1985**, 41, 244–247.
- (25) Hohenberg, P.; Kohn, W. Inhomogeneous electron gas. Phys. Rev. 1964, 136, B864.
- (26) Kresse, G.; Furthmüller, J. Efficient iterative schemes for ab initio total-energy calculations using a plane-wave basis set. *Phys. Rev. B: Condens. Matter Mater. Phys.* **1996**, *54*, 11169.
- (27) Kresse, G.; Joubert, D. From ultrasoft pseudopotentials to the projector augmented-wave method. *Phys. Rev. B: Condens. Matter Mater. Phys.* 1999, 59, 1758.
- (28) Gajdoš, M.; Hummer, K.; Kresse, G.; Furthmüller, J.; Bechstedt, F. Linear optical properties in the projector-augmented wave methodology. *Phys. Rev. B: Condens. Matter Mater. Phys.* **2006**, 73, No. 045112.
- (29) Perdew, J. P.; Burke, K.; Ernzerhof, M. Generalized gradient approximation made simple. *Phys. Rev. Lett.* **1996**, *77*, 3865.
- (30) Rohrbach, A.; Hafner, J.; Kresse, G. Electronic correlation effects in transition-metal sulfides. *J. Phys.: Condens. Matter* **2003**, *15*, 979
- (31) Jain, A.; Ong, S.; Hautier, G.; Chen, W.; Richards, W.; Dacek, S.; Cholia, S.; Gunter, D.; Skinner, D.; Ceder, G.; Persson, K.; equal contributions. The Materials Project: A materials genome approach to accelerating materials innovation. *APL Mater.* **2013**, *1*, No. 011002, Materials Project IDs: mp-1395638, mp-1296598, mp-1768665, mp-1752536.
- (32) Dudarev, S. L.; Botton, G.; Savrasov, S.; Humphreys, C.; Sutton, A. Electron-energy-loss spectra and the structural stability of nickel oxide: An LSDA+U study. *Phys. Rev. B: Condens. Matter Mater. Phys.* 1998, 57, 1505.
- (33) Blöchl, P. E. Projector augmented-wave method. *Phys. Rev. B: Condens. Matter Mater. Phys.* **1994**, *50*, 17953.
- (34) See Supporting Information.
- (35) Chamberland, B. A study on the NiVO<sub>3</sub> system. J. Solid State Chem. 1970, 2, 521–524.
- (36) Schindler, M.; Hawthorne, F.; Baur, W. Crystal chemical aspects of vanadium: polyhedral geometries, characteristic bond valences, and polymerization of (VO<sub>n</sub>) polyhedra. *Chem. Mater.* **2000**, *12*, 1248–1259.
- (37) Waroquiers, D.; Gonze, X.; Rignanese, G.-M.; Welker-Nieuwoudt, C.; Rosowski, F.; Göbel, M.; Schenk, S.; Degelmann, P.; André, R.; Glaum, R.; Hautier, G. Statistical analysis of coordination environments in oxides. *Chem. Mater.* **2017**, 29, 8346–8360.
- (38) Shannon, R.; Calvo, C. Refinement of the crystal structure of low temperature Li<sub>3</sub>VO<sub>4</sub> and analysis of mean bond lengths in phosphates, arsenates, and vanadates. *J. Solid State Chem.* **1973**, *6*, 538–549.
- (39) Bosi, F. Bond valence at mixed occupancy sites. I. Regular polyhedra. *Acta Crystallogr., Sect. B: Struct. Sci., Cryst. Eng. Mater.* **2014**, 70, 864–870.

- (40) Hryha, E.; Rutqvist, E.; Nyborg, L. Stoichiometric vanadium oxides studied by XPS. Surf. Interface Anal. 2012, 44, 1022–1025.
- (41) Silversmit, G.; Depla, D.; Poelman, H.; Marin, G. B.; De Gryse, R. Determination of the V2p XPS binding energies for different vanadium oxidation states (V<sup>5+</sup> to V<sup>0+</sup>). *J. Electron Spectrosc. Relat. Phenom.* **2004**, 135, 167–175.
- (42) Mendialdua, J.; Casanova, R.; Barbaux, Y. XPS studies of  $V_2O_5$ ,  $V_6O_{13}$ ,  $VO_2$  and  $V_2O_3$ . J. Electron Spectrosc. Relat. Phenom. 1995, 71, 249–261.
- (43) Bondarenka, V.; Grebinskij, S.; Kaciulis, S.; Mattogno, G.; Mickevicius, S.; Tvardauskas, H.; Volkov, V.; Zakharova, G. XPS study of vanadium—yttrium hydrates. *J. Electron Spectrosc. Relat. Phenom.* **2001**, *120*, 131–135.
- (44) Oswald, S.; Brückner, W. XPS depth profile analysis of non-stoichiometric NiO films. Surf. Interface Anal. 2004, 36, 17–22.
- (45) David, R.; Kabbour, H.; Bordet, P.; Pelloquin, D.; Leynaud, O.; Trentesaux, M.; Mentré, O. Triple Co<sup>II,III,IV</sup> charge ordering and spin states in modular cobaltites: a systematization through experimental and virtual compounds. *J. Mater. Chem. C* **2014**, *2*, 9457–9466.
- (46) Euzen, P.; Leone, P.; Mansot, J.; Bonneau, P.; Palvadeau, P.; Queignec, M. Synthesis and structural studies of manganese oxyhalides with a multisite framework: Part two: Mn<sub>7.5</sub>O<sub>10</sub>Br<sub>3</sub>, a new lacunar oxybromide. *Mater. Res. Bull.* **1992**, 27, 1423–1430.
- (47) Gillot, B.; Kharroubi, M.; Metz, R.; Legros, R.; Rousset, A. Electrical properties and cationic distribution in cubic nickel manganite spinels  $Ni_xMn_{3-x}O_4$ , 0.57 < x < 1. Solid State Ionics 1991, 44, 275–280.
- (48) Gillot, B.; Legros, R.; Metz, R.; Rousset, A. Electrical conductivity of copper and nickel manganites in relation with the simultaneous presence of Mn<sup>3+</sup> and Mn<sup>4+</sup> ions on octahedral sites of the spinel structure. *Solid State Ionics* **1992**, *51*, 7–9.
- (49) Godillot, G.; Guerlou-Demourgues, L.; Taberna, P.-L.; Simon, P.; Delmas, C. Original conductive nano-Co<sub>3</sub>O<sub>4</sub> investigated as electrode material for hybrid supercapacitors. *Electrochem. Solid-State Lett.* **2011**, *14*, A139–A142.
- (50) Gueho, C.; Giaquinta, D.; Mansot, J.; Ebel, T.; Palvadeau, P. Structure and magnetism of  $La_4Mn_5Si_4O_{22}$  and  $La_4V_5Si_4O_{22}$ : Two new rare-earth transition metal sorosilicates. *Chem. Mater.* **1995**, 7, 486–492.
- (51) Mansot, J.; Leone, P.; Euzen, P.; Palvadeau, P. Valence of manganese, in a new oxybromide compound, determined by means of electron energy loss spectroscopy. *Microsc., Microanal., Microstruct.* **1994**, *5*, 79–90.
- (52) Nemrava, S.; Vinnik, D. A.; Hu, Z.; Valldor, M.; Kuo, C.-Y.; Zherebtsov, D. A.; Gudkova, S. A.; Chen, C.-T.; Tjeng, L. H.; Niewa, R. Three Oxidation States of Manganese in the Barium Hexaferrite BaFe<sub>12-x</sub>Mn<sub>x</sub>O<sub>19</sub>. *Inorg. Chem.* **2017**, *56*, 3861–3866.
- (53) Wong, C. J.; Hopkins, E. J.; Prots, Y.; Hu, Z.; Kuo, C.-Y.; Pi, T.-W.; Valldor, M. Anionic ordering in Ba<sub>15</sub>V<sub>12</sub>S<sub>34</sub>O<sub>3</sub>, Affording three oxidation states of vanadium and a quasi-one-dimensional magnetic lattice. *Chem. Mater.* **2016**, *28*, 1621–1624.
- (54) Feng, S.; Yuan, H.; Shi, Z.; Chen, Y.; Wang, Y.; Huang, K.; Hou, C.; Li, J.; Pang, G.; Hou, Y. Three oxidation states and atomic-scale p—n junctions in manganese perovskite oxide from hydrothermal systems. *J. Mater. Sci.* **2008**, *43*, 2131–2137.
- (55) Li, M.; Huang, K.-K.; Chu, X.-F.; Du, Y.-Y.; Ge, L.; Sun, Y.; Hou, C.-M.; Feng, S.-H. Preparation of perovskite manganites with three oxidation states via the molten hydroxide method. *Chem. J. Chin. Univ.* **2013**, *34*, 284–287.
- (56) Shaju, K. M.; Guerlou-Demourgues, L.; Godillot, G.; Weill, F.; Delmas, C. Strategies for synthesizing conductive spinel cobalt oxide nanoparticles for energy storage applications. *J. Electrochem. Soc.* **2012**, *159*, No. A1934.
- (57) Godillot, G.; Huo, H.; Ménétrier, M.; Bourgeois, L.; Guerlou-Demourgues, L.; Delmas, C. Promising nanometric spinel cobalt oxides for electrochemical energy storage: investigation of Li and H environments by NMR. *J. Phys. Chem. C* **2012**, *116*, 26598–26607.
- (58) Godillot, G.; Guerlou-Demourgues, L.; Croguennec, L.; Shaju, K.; Delmas, C. Effect of temperature on structure and electronic

properties of nanometric spinel-type cobalt oxides. J. Phys. Chem. C 2013, 117, 9065–9075.

- (59) Kubelka, P.; Munk, F. An article on optics of paint layers. Z. Tech. Phys. 1931, 12, 259–274.
- (60) Tauc, J.; Grigorovici, R.; Vancu, A. Optical properties and electronic structure of amorphous germanium. *Physica Status Solidi B* **1966**, *15*, 627–637.
- (61) Makuła, P.; Pacia, M.; Macyk, W. How to correctly determine the band gap energy of modified semiconductor photocatalysts based on UV–Vis spectra. *J. Phys. Chem. Lett.* **2018**, *9*, 6814–6817.
- (62) Fritsch, V.; Hemberger, J.; Büttgen, N.; Scheidt, E.-W.; von Nidda, H.-A. K.; Loidl, A.; Tsurkan, V. Spin and orbital frustration in  $MnSc_2S_4$  and  $FeSc_2S_4$ . *Phys. Rev. Lett.* **2004**, *92*, No. 116401.
- (63) Tristan, N.; Zestrea, V.; Behr, G.; Klingeler, R.; Büchner, B.; von Nidda, H. K.; Loidl, A.; Tsurkan, V. Spin frustration and magnetic exchange in cobalt aluminum oxide spinels. *Phys. Rev. B: Condens. Matter Mater. Phys.* **2008**, 77, No. 094412.
- (64) Ghara, Ś.; Ter-Oganessian, N.; Sundaresan, A. Linear magnetoelectric effect as a signature of long-range collinear antiferromagnetic ordering in the frustrated spinel CoAl<sub>2</sub>O<sub>4</sub>. *Phys. Rev. B: Condens. Matter Mater. Phys.* **2017**, *95*, No. 094404.
- (65) Plumb, K.; Morey, J.; Rodriguez-Rivera, J.; Wu, H.; Podlesnyak, A.; McQueen, T.; Broholm, C. Antiferromagnetic and Orbital Ordering on a Diamond Lattice Near Quantum Criticality. *Phys. Rev. X* **2016**, *6*, No. 041055.

# Recommended by ACS

Switching between Proper and Hybrid-Improper Polar Structures via Cation Substitution in  $A_2La(TaTi)O_7$  (A = Li, Na)

Subhadip Mallick, Michael A. Hayward, *et al.*MARCH 31, 2021
CHEMISTRY OF MATERIALS

READ 🗹

# Physical Properties and Structural Stability of Cobalt Pyrovanadate ${\rm Co}_2{\rm V}_2{\rm O}_7$ under High-Pressure Conditions

Daniel Diaz-Anichtchenko, Catalin Popescu, et al.

JULY 28, 2022

THE JOURNAL OF PHYSICAL CHEMISTRY C

READ 🗹

# Pressure-Induced Transitions in the 1-Dimensional Vanadium Oxyhydrides $\rm Sr_2VO_3H$ and $\rm Sr_3V_2O_5H_2$ , and Comparison to 2-Dimensional $\rm SrVO_2H$

Takafumi Yamamoto, John E. McGrady, et al.

OCTOBER 28, 2019
INORGANIC CHEMISTRY

READ 🗹

# V–V Dimerization and Magnetic State of Cobalt Ions in Ilmenite-Type ${\rm CoVO_3}$

Sachiko Kamiyama, Hajime Yamamoto, et al.

MAY 09, 2022

INORGANIC CHEMISTRY

READ 🗹

Get More Suggestions >